

Insights into Material Design, Extrusion Rheology, and Properties of 3D-Printable Alkali-Activated Fly Ash-Based Binders

Hussam Alghamdi¹, Sooraj A. O. Nair², Narayanan Neithalath^{3,*}

Abstract

Material design of alkali activated fly ash-based binders for extrusion-based 3D printing, the rheological responses that are influential in ensuring printability, and the properties of such binders are discussed in this paper. Fly ash is supplemented with fine limestone, slag, or portland cement to provide adequate microstructural packing required for printability. The alkaline activators help reduce the yield stress and enhance the cohesiveness of the mixtures. Based on the measured shear yield stress at different times and concurrent printing of a filament, the printability window and yield stress bounds for printability, applicable for the chosen printing parameters, are established. This approach could be used for mixture qualification for extrusion-based printing. The Benbow-Bridgwater model is implemented on extrusion rheology results of pastes to determine the extrusion yield stress and wall slip shear stress, which are useful process-related parameters. It is shown that these parameters can also be related to shear and extensional rheological properties of alkali-activated pastes, thus ensuring a much-needed link between parameters related to material design and the process of extrusion. Mechanical properties and pore structure similar to those of conventionally cast mixtures are achieved.

Keywords: 3D printing; Alkali activation; Fly ash; Extrusion rheology; Yield stress.

¹ Graduate student, School of Sustainable Engineering and Built Environment, Arizona State University, Tempe AZ 85287

² Graduate student, School of Sustainable Engineering and Built Environment, Arizona State University, Tempe AZ 85287

^{3,*} Professor, School of Sustainable Engineering and Built Environment, Arizona State University, Tempe AZ 85287; Corresponding Author (Phone: +1-480-965-6023; Fax: +1-480965-0557; e-mail: Narayanan.Neithalath@asu.edu)

25 1. Introduction

26 3D printing (or additive manufacturing) enables fabrication of complex and multi-scale structures through
27 computer-aided design [1,2]. This technology has been successfully applied in aerospace, automotive, and
28 biomedical fields [3–5]. 3D printing of cementitious materials where structures are created by layer-wise
29 construction enables acceleration of the construction process, helps build complex architectural shapes
30 that otherwise are difficult to realize, and facilitates labor and energy reductions [6–10]. 3D printing also
31 enables special components to be fabricated. As an example, low cost syntactic foams (hollow particles
32 filled composite materials) were recently created by 3D printing technique as reported in [11,12]. The
33 commonly used 3D printing technique for concrete is material extrusion and layered printing [8,13–15],
34 even though direct ink writing and powder-based printing have also been attempted [16–19]. These mixes
35 are designed to flow through a barrel-die system and have enough structural stability when stacked in
36 layers to print a stable structure. In extrusion-based printing, the rheological characteristics of the
37 mixtures play a crucial role, and thus several studies have explored the influence of paste rheology in 3D
38 printing of cementitious materials [19–23]. In addition to rheological properties, setting time and
39 mechanical properties of the printed elements are also of interest [24,25], as is the case with any
40 construction material.

41 A large number of ongoing studies on 3D printing of cementitious materials focus on the use of binders
42 based on ordinary portland cement (OPC), as expected [9,26,27]. Significant advances in the field of
43 mineral and chemical admixtures have aided in the production of OPC-based 3D printed materials whose
44 rheology and early-age response can be tailored. The use of geopolymer binders, which has been widely
45 recognized as a sustainable option to reduce the carbon footprint of concrete, for 3D printing has also
46 been reported [28–32]. It is conceivable that such sustainable binders can be utilized in mass construction,
47 especially in areas where waste/by-product materials like fly ash are abundant. 3D printing of low strength
48 geopolymer binders can also be employed in disaster rehabilitation where temporary structures are
49 needed. This paper examines the aspects that are relevant in the material design of fly ash-based alkali
50 activated binders for 3D printing. Special focus is given to: (i) the use of minor ingredients including fine
51 limestone powder that contributes to improved microstructural packing that provides the network
52 strength in the fresh state to be extruded and layered in a shape-stable manner, and (ii) the influence of
53 alkaline activators on the rotational, extensional, and extrusion rheology of pastes. These studies
54 elucidate the relevant characteristics of the fresh pastes that are influential in printability. Extrusion
55 rheology experiments combined with phenomenological modeling is used to obtain the linkage between

56 the material design and process-related parameters, thereby enabling better strategies to produce
 57 sustainable, alkali-activated 3D printable binder systems.

58 **2. Experimental Program**

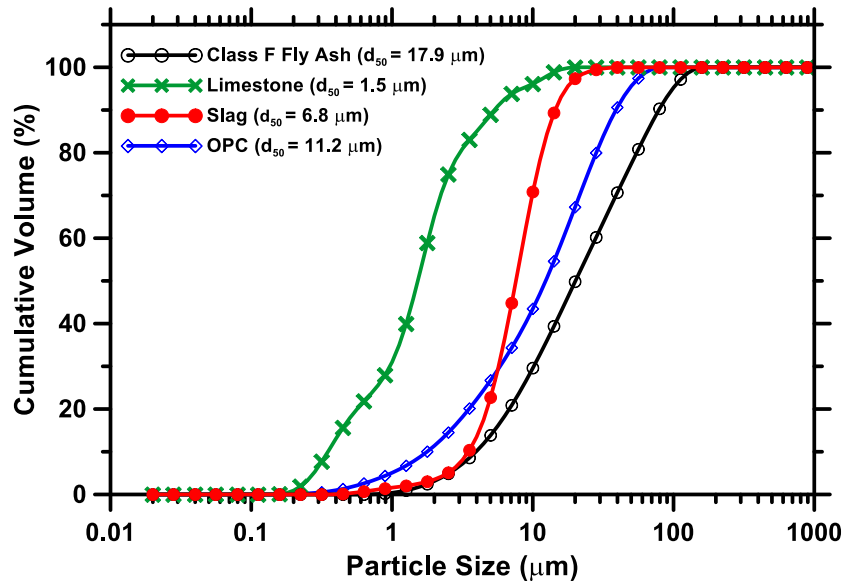
59 **2.1 Source Materials and Activators**

60 The primary source material utilized in this study was class F fly ash conforming to ASTM C 618. Based on
 61 our previous work [20] and several trial mixtures, it was observed that other minor ingredients are
 62 required to ensure extrudability and buildability (together termed as printability). Moreover, materials
 63 such as slag and ordinary portland cement (OPC), when incorporated into alkali activated fly ash-based
 64 systems, improves the setting time and the mechanical properties of the binder. Table 1 lists the binder
 65 components utilized in this study, along with their chemical composition. Figure 1 shows the particle size
 66 distributions (PSDs) of the source materials used. Sodium hydroxide (NaOH), sodium silicate solution
 67 (waterglass), or sodium sulfate (Na₂SO₄) were used as the activating agents in this study. NaOH was used
 68 as the sole activator, or in combination with sodium silicate or sodium sulfate to provide requisite
 69 alkalinity to enable aluminosilicate dissolution and precipitation. Waterglass supplied by PQ Corporation
 70 has a solids content of 36%, a silica modulus (molar ratio of SiO₂-to-Na₂O) (M_s) of 3.3, and specific gravity
 71 of 1.38 g/cm³. The sodium hydroxide and sodium sulfate powders were determined to have specific
 72 gravities of 2.13 and 2.66 g/cm³ respectively.

Table 1: Chemical composition of the source materials

Components of the binders	Chemical composition (% by mass)						
	SiO ₂	Al ₂ O ₃	Fe ₂ O ₃	CaO	MgO	SO ₃	LOI
Fly ash (F)	58.40	23.80	4.19	7.32	1.11	3.04	2.13
Slag (S)	36.0	10.5	0.67	39.8	7.93	2.10	3.01
OPC (C)	19.60	4.09	3.39	63.21	3.37	3.17	2.54
Limestone (L)	CaCO ₃ > 99%						
Alumina powder (A)	AL ₂ O ₃ > 99%						

73



74

75

Figure 1: Particle size distributions (PSD) of the paste constituents.

76

2.2 Printer and Print Geometries

77

A desktop printer based on Cartesian configuration [33] was customized with a 100 cm³ barrel to print the alkali activated paste mixtures. The diameter of the barrel (D_b) used for paste printing was 35 mm. Two different die exit diameters were adopted in this study (4 mm and 6 mm) with lengths of 35 mm and 20 mm respectively to maintain the die length-to-diameter ratios (L_d/D_d) of 9 and 3.33. The die entry diameter was 10 mm. The inner surface of barrel was lubricated to reduce the wall friction and ensure smooth and easy motion of the piston. Several shapes were printed to investigate and visually inspect the printability of mixtures. Slic3r software [34] was used to adjust the printing parameters including printing speed, layer width and height, and infill volume and pattern. The printing parameters used in this study are: layer height of 3mm, layer width of 6 mm, and printing speed of 20 mm/s.

76

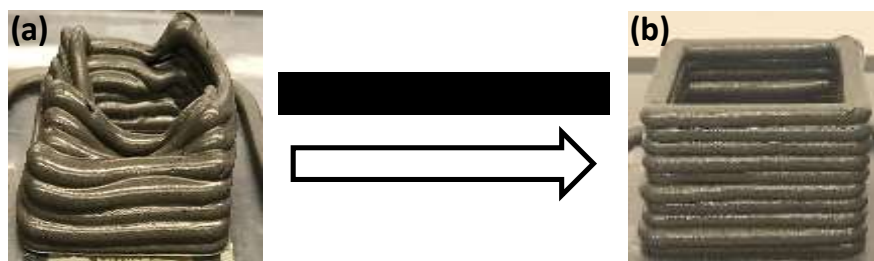
2.3 Material Design for Printability: Multi-Component Binders and Activators

77

The printability criteria employed in this study were: (i) the ease of extrusion through a tapered nozzle (extrudability), and (ii) the stability of the layered printed shape (buildability). These criteria, together termed as printability, were visually ascertained in the preliminary phase of the study to select a matrix of alkali-activated fly ash-based mixtures for 3D printing. The extrudability and buildability of the selected mixtures are quantified later. Note that these are also dependent on printing parameters including nozzle shape and printing speed. The material design procedure started with class F fly ash as the sole binder, activated by a 5% NaOH solution. Mixtures were prepared using a mass-based liquid-to-binder ratio (l/b)

93

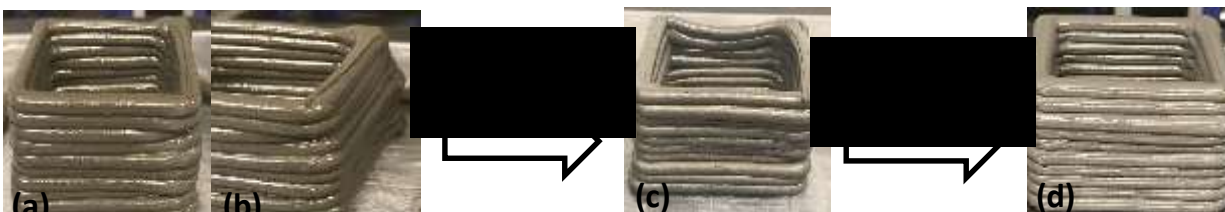
94 starting from 0.20, at 0.01 increments. Mixtures developed using the lower end of this l/b range were very
95 stiff and difficult to extrude. A l/b of 0.25 was found to result in a cohesive, extrudable paste (control
96 mixture); however, this mixture was not buildable, as shown in Figure 2(a). This response is similar to that
97 observed for plain OPC and OPC-fly ash pastes reported in [20], which were also not buildable. The
98 buildability of the cement pastes, for a given set of printing parameters, is a strong function of the initial
99 yield stress of the paste, which depends on the number and quality of interparticle contacts. This in turn,
100 is a function of the particle sizes, arrangement of the particles (including effects of flocculation), and the
101 type of interparticle forces [35]. However, flocculation and its effects are not discussed in this paper. The
102 use of fly ash (d_{50} of $\sim 18 \mu\text{m}$) alone as the binder is likely to result in an insufficient number of interparticle
103 contacts to provide sufficient yield stress to the paste. Thus, fine limestone (d_{50} of $1.5 \mu\text{m}$) was used as a
104 filler material [36], replacing 15% of fly ash by mass, to enhance the number of interparticle contacts in a
105 given volume and give better fresh state rigidity to the system to resist the overburden pressure without
106 instability. The printability was substantially improved through this minor compositional change, as shown
107 in Figure 2(b). The l/b was increased to 0.27 to ensure extrudability, attributable to the presence of fine
108 limestone particles.



109
110 Figure 2: Hollow cube geometry printed using fly ash-based binders activated using 5% NaOH: (a) 100%
111 class F fly ash paste ($l/b=0.25$), showing shape instability, and (b) improvement in printability and
112 buildability when 15% fine limestone is incorporated into the paste ($l/b=0.27$).

113 Next, the activator concentration was increased from 5% to 10% NaOH. With a 10% NaOH content in the
114 activator solution, an extrudable mixture containing fly ash alone was obtained with a l/b of 0.20 (as
115 compared to a l/b of 0.25 for 5% NaOH activation). The increase in activator viscosity with increase in
116 NaOH concentration enhances the cohesiveness of the mixture [37]. The combined effects of: (i) reduced
117 interparticle spacing at a lower l/b, (ii) increased activator viscosity, and (iii) greater negative surface
118 charges on fly ash particles at higher NaOH concentrations that result in increased interparticle repulsion
119 [37] enable the production of an extrudable mixture as shown in Figure 3(a) and (b), at a l/b of 0.20.
120 However, the mixture was too cohesive, to the extent of being very “sticky”, that resulted in layer

121 deformation at corners during the printing process (as the print head drags already laid material), as can
122 be noticed in these figures. To compensate for this effect, the l/b was increased to 0.24, along with the
123 replacement of 15% of fly ash with fine limestone powder. Figure 3(c) shows that, while the mixture
124 consistency and water retention was improved (note the shine in Figure 3(a) and (b), which is due to water
125 draining from the paste, while Figure 3(c) shows improved water retention due to limestone addition),
126 the print quality was still inconsistent. Minor compositional changes could account for these effects, but
127 in order to create a more diverse composition, the limestone content was increased to 30%, and the l/b
128 to 0.27, to result in a satisfactorily extrudable and buildable mixture as shown in Figure 3(d). Note that
129 the l/b is same for the selected mixtures with 15% and 30% limestone powder (Figure 2(b) and 3(d)). It has
130 been suggested that higher hydroxide contents in particulate suspensions might have an effect similar to
131 that of superplasticizers [37].



132 Figure 3: Hollow cube geometry printed using fly ash-based binders activated using 10% NaOH: (a and b)
133 100% Class F fly ash paste (l/b=0.20) showing layer deformation, (c) binder with 15% limestone
134 (l/b=0.24), showing shape instability, and (d) binder with 30% limestone (l/b=0.27) showing satisfactory
135 printability and buildability.
136

137 In addition to the binary fly ash – limestone systems discussed earlier, slag or OPC were also used as
138 components of the activated binders to develop ternary blend systems. In such cases, the fly ash content
139 was fixed at 50% (mass-based). The fly ash – OPC – limestone system was activated by a combination of
140 sodium sulfate and NaOH so as to reduce the overall alkalinity of the activator and ensure easier handling.
141 It has been shown that Na₂SO₄ (a neutral salt) activation of high volume fly ash mixtures result in 28-day
142 compressive strengths of ~30 MPa when cured at ambient temperatures [38]. The addition of 1% NaOH
143 enhanced the cohesiveness of this system. The fly ash – slag – limestone system was activated using NaOH
144 or a combination of NaOH and sodium silicate to provide a Na₂O-to-powder ratio (n) of 0.05 and SiO₂-to-
145 Na₂O ratio of the activator (M_s) of 0.50. In the latter system, 1% Al powder was used to delay the setting
146 time of the mixture. The chosen mixtures were mixed at 200 rpm for 30 seconds, followed by 1200 rpm
147 for 90 seconds to obtain a homogenous mixture. Table 2 lists the selected binders used for further studies.
148 Note that the letter (F, L etc.) corresponds to the ingredients (see Table 1), and the number in the subscript
149 refers to the mass fraction of the ingredient in the starting binder blend. The median particle sizes of

150 blends are also listed in the table to indicate how the use of minor ingredients change d_{50} of the composite
 151 mixture. This is significant since yield stress is known to be well related to the square of d_{50} [20,35].

Table 2: Binder proportions and the median particle sizes (d_{50}) for the final printable mixtures

Mixture ID	FFA (%)	Slag (%)	OPC (%)	LS (%)	Al powder (%)	Alkali activator (%)		Liquid/powder ratio	d_{50} (μm)
						NaOH (%)	Na ₂ SO ₄ (%)		
F ₈₅ L ₁₅	85			15		5		0.27	15.20
F ₇₀ L ₃₀	70			30		10		0.27	10.37
F ₅₀ C ₃₀ L ₂₀	50		30	20		1	2	0.30	11.32
F ₅₀ S ₃₀ L ₂₀	50	30		20		5		0.35	8.79
F ₅₀ S ₃₀ L ₁₉ A ₁	50	30		19	1	n=0.05*, M _s =0.5**		0.30	8.71

* n= Na₂O/total powder (mass based); NaOH is the source of Na₂O.

** M_s= SiO₂/Na₂O (molar based), Sodium silicate solution is the source of SiO₂.

152

153 **2.4 Test Methods**

154 **2.4.1 Rheological characterization**

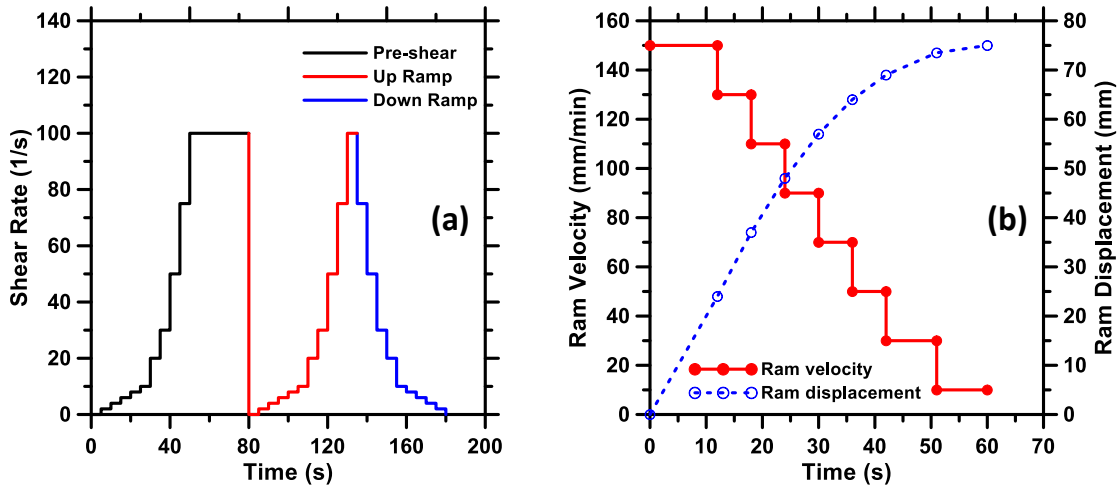
155 A mini slump cone with a bottom diameter of 38 mm, top diameter of 19 mm, and a height of 57 mm was
 156 used to determine the shape stability of the printable binders. The paste was loaded in the mini-slump
 157 cone and then slowly lifted to determine the slump value. A dynamic shear rheometer (TA Instruments
 158 AR 2000EX) was used to carry out the rheological studies using a parallel plate geometry to determine the
 159 shear stress (τ) of the printable pastes as a function of shear rate ($\dot{\gamma}$). The upper and lower plates were
 160 serrated at depths of 1 mm and 0.15 mm respectively to prevent paste slip on the shearing surface. The
 161 bottom plate contained Peltier elements, and was conditioned to a temperature of 25 ± 0.1 °C. The
 162 volume of paste sample was calculated for a plate gap of 2 mm and evenly put on the bottom plate to
 163 avoid an overfilled state while testing. The sequence of steps employed in rotational parallel plate
 164 rheology includes: (i) a stepped ramp up pre-shear phase for approximately 80 s to homogenize the paste,
 165 (ii) a stepped ramp-up, and (iii) a stepped ramp-down, as shown in Figure 4(a) [36,39]. The data was
 166 collected from only the down-ramp phase. Shear stress and shear rate data were extracted using TA
 167 Instruments' TRIOS software package. The range of the shear rate used in this test were from 5-to-100 s⁻¹,
 168 and the Bingham model was used to extract the apparent yield stress from the relationship between
 169 shear stress and shear strain rate. In addition to shear rheology, the parallel plate test set up was also
 170 used for the tack test. The tack test indicates the adhesive properties and cohesion of the paste mixtures.
 171 These properties are important to ensure that the pastes adhere well to surfaces, which influences the

172 interface properties [40]. The paste was placed on the bottom plate and a gap of 2 mm was set between
 173 the plates. A pre-shear phase similar to the one shown in Figure 4(a) was used to homogenize the paste.
 174 The top plate was set to rise at a constant velocity of 10 μm/s until the sample was completely separated
 175 from the plates. The normal force experienced by the top plate was recorded as a function of plate
 176 separation.

177 A 4.45 kN servo-controlled MTS machine was used to carry out the extrusion rheology studies of alkali
 178 activated printable pastes. The paste sample was filled in the extruder immediately after mixing, ensuring
 179 that no air voids are entrapped in the paste. The plunger was placed inside the barrel in direct contact
 180 with the compacted paste. The assembly was placed in a specially fabricated holder to allow the upper
 181 platen of the test machine to axially compress the plunger. A multi-speed extrusion test with ram
 182 velocities ranging from 150 mm/min to 10 mm/min was used. Figure 4(b) shows the experimental
 183 procedure used for the extrusion rheology tests. The nozzle (die) diameters used for the extrusion test
 184 were 4 mm and 6 mm, and the corresponding nozzle lengths were 35 mm and 20 mm respectively. The
 185 extrusion velocity is calculated from the ram velocity using flow equivalence, given as:

$$186 \quad D_b^2 V_{ram} = D_d^2 V_{ext} \quad (1)$$

187 where V_{ram} is the ram velocity and V_{ext} is the extrusion velocity, and D_b and D_d are the barrel and die
 188 diameters respectively.



189
 190 Figure 4: Experimental procedure used for: (a) parallel plate rheology, (b) extrusion test.

191 **2.4.2 Pore structure and mechanical properties**

192 The setting times of the selected mixtures were determined in accordance with ASTM C 191-18a [41],
 193 with a time gap between each penetration reading of 15 minutes. Mercury intrusion porosimetry (MIP)

194 was used to investigate the porosity and critical pore sizes of the different layers of the printed pastes.
195 Small samples carefully obtained from different printed layers were placed in the low-pressure chamber
196 of the porosimeter (Quantachrome Instruments Pore Master). The sample was pressurized with mercury
197 from an ambient pressure to 345 KPa (60 psi). This is followed by intrusion of mercury in a high-pressure
198 chamber where the pressure was increased to 414 MPa (60,000 psi). The pore diameter (d) as a function
199 of the intrusion pressure can be obtained from the Washburn equation as:

$$200 \quad d = \frac{-4 \sigma \cos\theta}{\Delta P} \quad (2)$$

201 where ΔP is the difference in the pressure between successive steps (MPa), θ is the contact angle
202 between mercury and the cylindrical pore (130° in this study) [42–44], and (σ) is the surface tension
203 between mercury and the pore walls (485 mN/m).

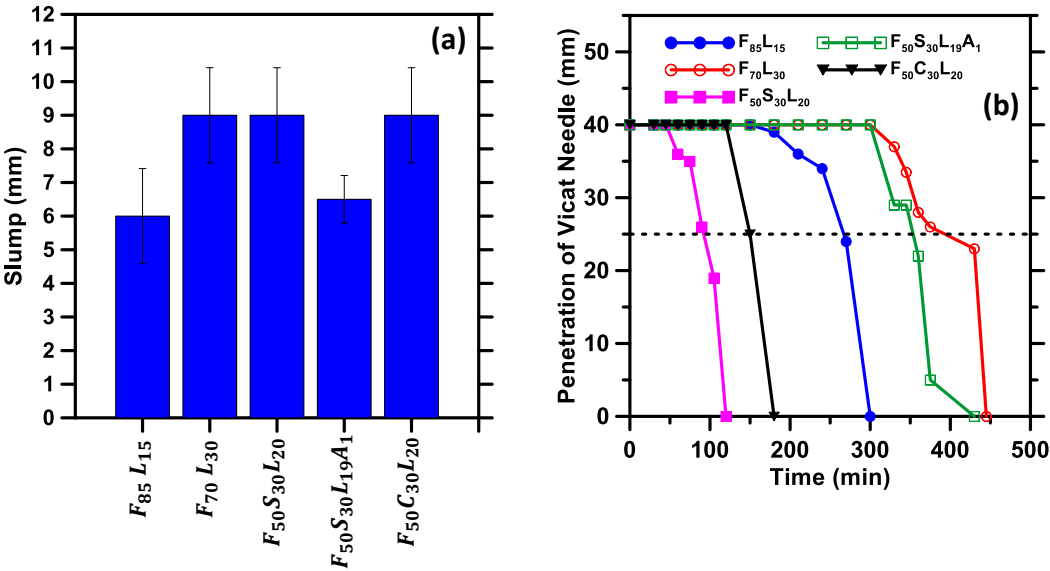
204 The specific gravities of the paste samples were determined using a gas pycnometer (Ultrapyc 1200e,
205 Quantachrome Instruments). The compressive strengths of the printed pastes were determined on
206 printed cubes of 40 mm side length. The flexural strength of the printed pastes was determined using a
207 three-point-bending test. A displacement rate of 0.5 mm/min was used for the tests [45]. Three replicate
208 specimens 21 mm x 21 mm x 120 mm in size were tested for each mixture listed in Table 2.

209 **3. Results and Discussions**

210 **3.1 Mini-Slump Flow and Initial Setting Times**

211 The **workability** of the pastes and their setting times are important parameters in the qualification of 3D
212 printable binders. Sufficiently long initial setting time is necessary to avoid premature stiffening while the
213 mixture is being extruded and printed. Figure 5(a) shows the mini slump values and Figure 5(b) shows the
214 needle penetration as a function of time for the selected paste mixtures. It is desirable to have a cohesive
215 mixture demonstrating minimal slump to obtain a stable print with little or no deformation while
216 maintaining extrudability. The maximum **mini-slump** value recorded was less than 9 mm which allowed
217 **consistent extrusion while being able to retain the shape during and after printing**. The initial setting time
218 ranged between 1.5 to 6.0 hours, which is generally attributed to the low reactivity of fly ash at ambient
219 temperatures. **For the mixtures (F₈₅L₁₅) and (F₇₀L₃₀), the setting time of (F₇₀L₃₀) was apparently delayed,**
220 **attributable to increased alkaline activator (10% of NaOH) used in this mixture compared to (5% of NaOH)**
221 **used in (F₈₅L₁₅). The increased NaOH decreased silica polymerization resulting in delayed setting time as**
222 **reported in [46]. For the slag or OPC containing mixtures (F₅₀S₃₀L₂₀, and F₅₀C₃₀L₂₀), the rapid setting was**

223 attributed to the presence of slag [47] and OPC which helped accelerate the setting time at ambient
 224 temperature. However, the mixture containing slag along with alumina ($F_{50}S_{30}L_{19}A_1$) showed the longest
 225 setting time of approximately 6 hours due to the presence of alumina that delayed the setting time as
 226 proved in literature [48]. The cohesiveness of the mixtures, attained through improved packing of particles
 227 [24,49] (Section 2.3), ensured that the printed shapes were stable.



228

229 Figure 5: (a) Slump values and (b) initial setting times of the printable pastes.

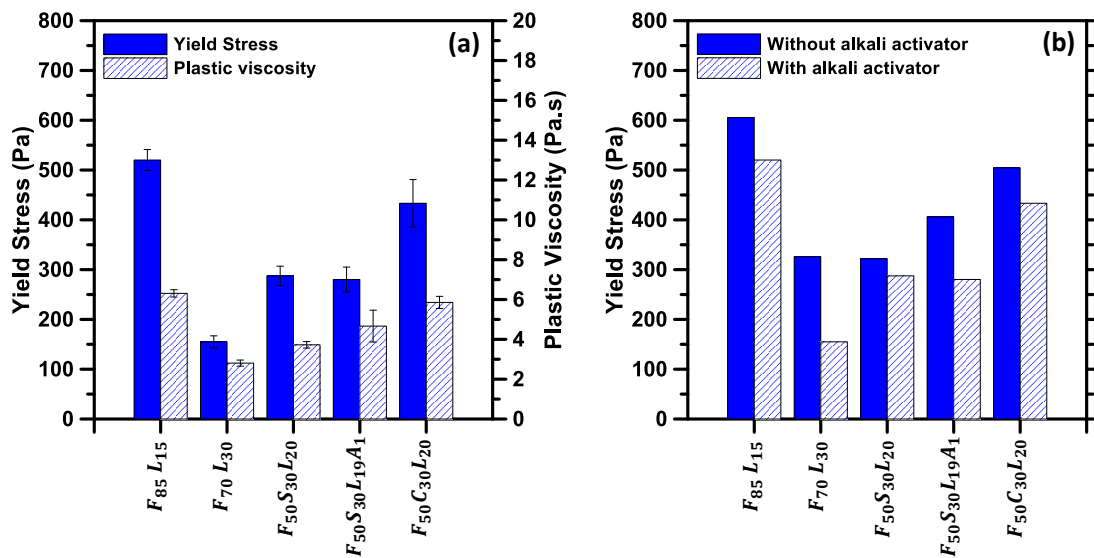
230 **3.2 Rheological Characterization of Fresh Pastes**

231 **3.2.1 Yield stress from parallel plate rheology and its relation to printability**

232 The yield stress of the pastes is influenced by the composition of the binders, and the type and amount
 233 of activators. Figure 6(a) shows the effect of mixture composition on the yield stress and plastic viscosity
 234 of the selected binders. The $F_{70}L_{30}$ mixture shows the lowest yield stress due to the higher amount of
 235 NaOH (10%) which acts like a superplasticizing admixture [37]. The yield stress of the $F_{85}L_{15}$ mixture is
 236 higher because of the lower water content in this mixture and the lower amount of NaOH. For mixtures
 237 containing 50% of fly ash, the yield stress and plastic viscosity are higher when OPC is present in the
 238 mixture than when slag is present. From the particle size distributions shown in Figure 1, it appears that
 239 OPC has a higher fraction of finer particles (0.5 to 5 μm) than slag, which could explain this behavior from
 240 a particle packing point of view. This is consistent with the inverse size dependence on yield stress shown
 241 in several studies (e.g. [50]). It is also conceivable that the surface charges in OPC that influence
 242 flocculation, and the effects of particle shapes might also play a role in this behavior. The yield stresses
 243 vary between 150 Pa and 500 Pa for all the mixtures evaluated, which is very similar to the extrudable and

244 printable OPC-based binders evaluated in a companion study [20]. As suggested earlier, this range
 245 depends on the printing parameters also.

246 It is instructive to understand the influence of the activating agents on the yield stress of suspensions.
 247 Hence the yield stress of the printable binders shown in Figure 6(a) are compared to those obtained when
 248 water is used as the dispersing medium instead of the alkaline solution. The results are shown in Figure
 249 6(b). The decrease in yield stress when alkaline activators are used as dispersing media can be attributed
 250 to the fact that alkaline solutions act in a manner similar to that of superplasticizers [37]. The higher the
 251 alkalinity of the activator, the larger the decrease in yield stress.

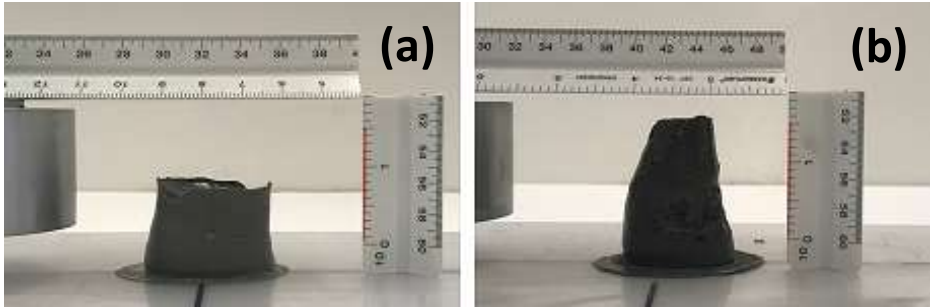


252
 253 Figure 6: (a) Yield stress and plastic viscosity of the printable binders, and (b) effect of alkali activators on
 254 yield stress of design printable fresh pastes.

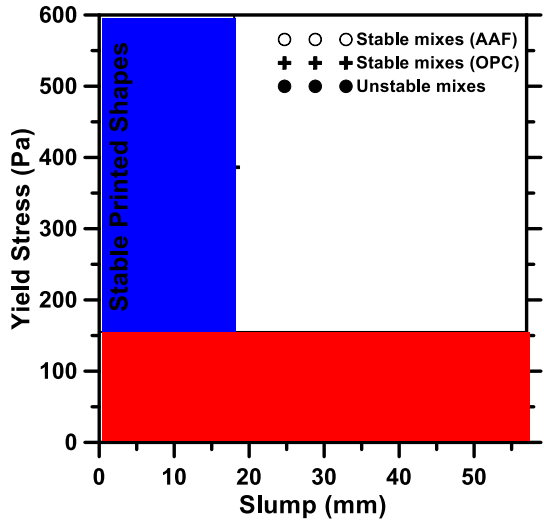
255 Figure 7(a) shows the mini slump test on an extrudable fly ash-water paste at an l/b of 0.25, while Figure
 256 7(b) shows an extrudable fly ash-water-NaOH paste at an l/b of 0.20. It can be seen that, in addition to
 257 decreasing the yield stress (even at a lower l/b ratio), alkaline solutions also resulted in enhanced
 258 cohesiveness of the pastes and better shape retention.

259 **Printability is defined as the ability of a mixture to extrude (extrudability) and maintain the structural**
 260 **integrity when built in layers (buildability) [51], as explained earlier.** Yield stress is an important rheological
 261 parameter that influences printability. It is also well known that slump of a cementitious mixture is related
 262 to its yield stress [52,53]. Thus, the use of mini slump values and the yield stress obtained from rotational
 263 rheology are synergistically considered to arrive at bounds for printability of the paste mixtures. Here, in
 264 addition to the alkali-activated binders considered in this paper, data from a companion work on OPC-

265 based binders [20] are also used. Figure 8 depicts the yield stress and slump of a range of mixtures
 266 considered, both printable and non-printable. All the considered mixtures were extrudable. A lower mini
 267 slump value and a higher yield stress are generally found to be the requirements for a printable mixture.



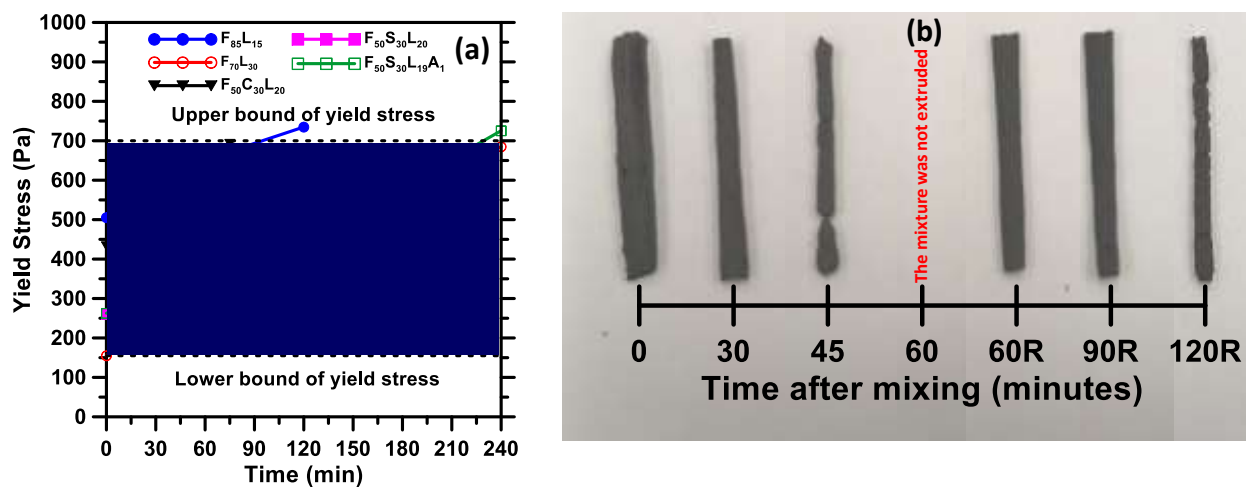
268
 269 Figure 7: Mini slump of 100% fly ash paste mixed with: (a) only water, and (b) water with 10% of NaOH
 270 showing the effect of alkaline activator on paste slump and its cohesiveness.



271
 272 Figure 8: Yield stress vs. slump value of printable and non-printable mixtures
 273 (Data for stable mixes (OPC) labelled in the graph was obtained from our previous study [20].

274 The evolution of yield stress with time provides useful indications on the window of printability. For all
 275 the selected mixtures, yield stress was determined using the parallel plate geometry after maintaining the
 276 paste at rest different periods of time, as shown in Figure 9(a). The time interval between two
 277 measurements were determined based on the setting time of the pastes (Figure 9(b)). For the pastes that
 278 set faster (i.e., the 50% fly ash mixtures containing slag or OPC), the yield stress was measured after a rest
 279 period of 30 minutes, while for the other mixtures, the first rest period was 60 minutes. Corresponding to
 280 every time interval of yield stress measurement, a single filament was extruded and printed at different
 281 times after initial mixing. An example is shown in Figure 9(b) for the F₈₅L₁₅ mixture. The yield stress of the
 282 mixture corresponding to the final time beyond which it cannot be extruded and printed is designated as

283 the upper bound of yield stress. For all the mixtures evaluated here, the yield stress limit of extrudability
 284 and printability was around 700 Pa (limited by the printer's capacity used in this study). In Figure 9(b), it
 285 is shown that, at 60 minutes (the time of first yield stress measurement for the $F_{85}L_{15}$ paste), remixing was
 286 done for 30 s before printing the filament again. This is to simulate the homogenization that happens
 287 during the pre-shear phase in the yield stress measurement method. The time from initial mixing to the
 288 time when the yield stress reaches approximately 700 Pa is termed as the printability window. Based on
 289 the above analysis, the $F_{70}L_{30}$ and $F_{50}S_{30}L_{19}A_1$ mixtures showed the longest printability window (3h) while
 290 the $F_{50}S_{30}L_{20}$ mixture showed the shortest window (1h). The printability window is found to scale relatively
 291 well with the initial setting time of the pastes, indicating that the setting time could be used as a surrogate
 292 parameter to estimate the printability window. This finding assumes significance since it shows that a
 293 simple test such as the setting time can be a useful indicator of an important process parameter, i.e.,
 294 printability window, relating to 3D printing. It is also important to note that this result has been arrived at
 295 based on the few selected mixtures from this study and extensive investigations are needed to ensure
 296 that the relationship is valid over a wide range of mixture compositions.



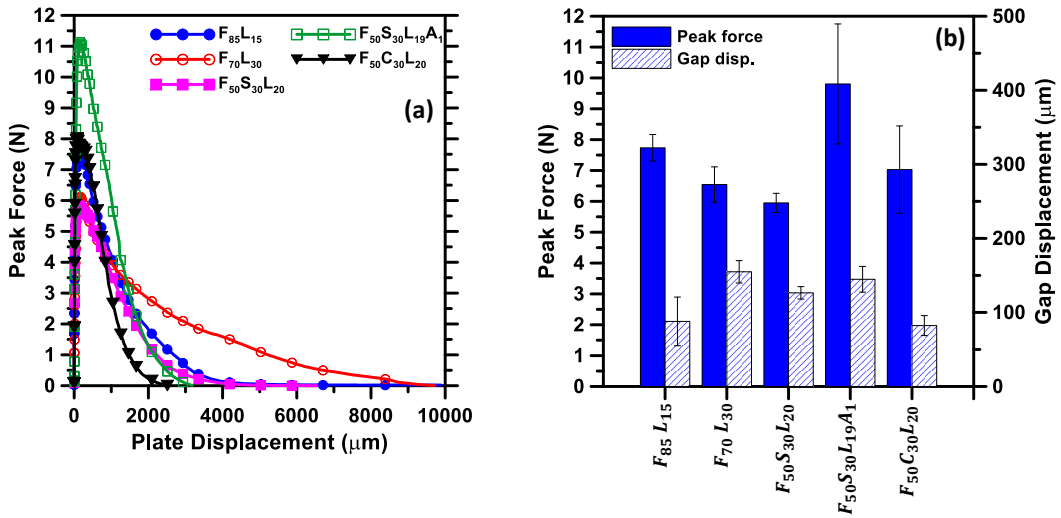
297
 298 Figure 9: (a) Yield stress of printable mixtures with time showing the printability zone, and (b) extruded
 299 filaments of $F_{85}L_{15}$ mixture as a function of time after mixing. (R: remixing for 30 s after 60 min from
 300 initial mixing time).

301 3.2.2 Tack test (extensional rheology)

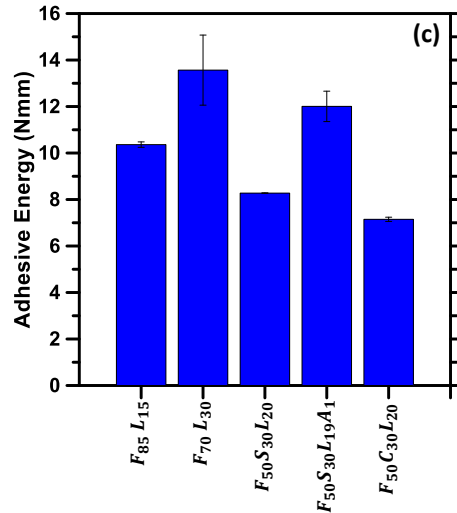
302 Extensional rheology can be used to quantify the adhesive and cohesive nature of the pastes, which are
 303 influential in 3D printing. Cohesion is defined as the internal strength of the material at rest while
 304 adherence is defined as the tendency of the material to stick to a surface [54]. These properties influence

305 the interlayer bonding in layered manufacturing, which plays an important role in the mechanical
 306 properties of the printed components.

307 Figure 10(a) shows the normal force as a function of plate displacement for the printable alkali-activated
 308 fly ash-based pastes, and Figure 10(b) shows the peak force and the gap displacement corresponding to
 309 the peak load. The adhesive and cohesive properties of the paste can be evaluated by the absolute value
 310 of the peak force and resistance of the paste to elastic failure [55]. An elastic increase in the normal force
 311 until the peak is demonstrated by all the mixtures. The peak load (corresponding to critical gap
 312 displacement) corresponds to the cohesion of the mixture beyond which rupture occurs and force starts
 313 to decay under a combination of viscous effects in adhesion and intrinsic cohesion. A higher peak force is
 314 reported to correspond to a higher adhesive capacity [55]. Figure 10(c) depicts the adhesion energy of the
 315 selected pastes, defined as the area under the force-displacement curve. The energy required to separate
 316 the paste under a normal tensile force is indicative of the influence of material composition on the
 317 bonding capacity, which influences interface properties of the 3D-printed structure.



318



319

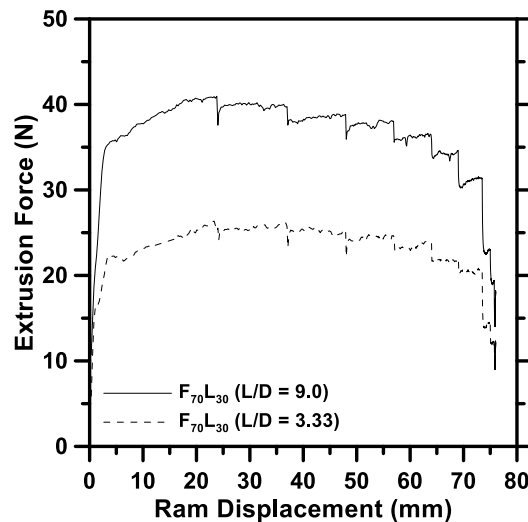
320 Figure 10: Tack test results showing: (a) absolute normal force as a function of plate displacement, (b)
 321 peak force and corresponding gap displacement for the selected pastes, and (c) adhesion energy of the
 322 design printable pastes.

323 The average peak forces of the selected pastes were between 6 N and 10 N whereas the total
 324 displacement (at complete separation) ranged between 2 to 9 mm (excluding the initial gap of 2 mm). The
 325 peak forces and the corresponding gap displacements shown in Figure 10(b) indicate that the paste
 326 containing OPC demonstrate the lowest gap displacement at peak force. This is corroborated by the
 327 lowest adhesive energy showed by this paste as shown in Figure 10(c). The lower gap displacement and
 328 the faster force decay after rupture indicates lower cohesive forces in the system containing OPC as
 329 compared to other mixtures evaluated. This can also be attributed to the lower alkalinity of the paste
 330 containing OPC – the higher viscosity of NaOH combined with its higher concentration in the other systems
 331 contributing to increased cohesive stresses in the fresh state. Further, the paste containing the highest
 332 amount of NaOH ($F_{70}L_{30}$) showed the highest adhesive energy among the mixture studied, once again
 333 emphasizing the influence of the activating agent characteristics on early age adhesive and cohesive
 334 forces. The adhesion energy of the alkali-activated fly ash-based pastes reported here are 1.2 to 2 times
 335 higher than that of the OPC-based pastes reported in our previous work [20]. While much of this is
 336 attributed to the activator characteristics as mentioned earlier, this has implications in interlayer
 337 properties when a wet-on-wet layer construction scheme is implemented, as is the case with 3D-printed
 338 cementitious structural elements. Also, higher modulus can result in a reduction of inter-layer bond
 339 strength [56] which is related to lower adhesive energy of the mixes.

340 3.3 Influence of the Extrusion Process on the Rheology of the Printed Material

341 The rheological response of fresh binder mixtures was reported in the preceding sections, and criteria
342 that could be used to infer important characteristics such as printability window, yield stress bounds, and
343 adhesive characteristics discussed. However, extrusion involves application of pressure on the fluid paste
344 at a certain velocity, and the rheological characteristics are highly sensitive to pressure and speed of
345 extrusion. Analytical models and numerical models to evaluate the behavior of a yield stress fluid under
346 pressure have been reported [57–61]. However, for ease of analysis and interpretation, we carry out
347 extrusion rheology and implement a phenomenological Benbow-Bridgwater model [61] to analyze paste
348 extrusion and infer the rheological characteristics of the extruded and printed material. The Benbow-
349 Bridgwater model employs a plasticity approach to analyze the extrusion rheology of dense ceramic
350 suspensions [62].

351 Figure 11 shows the extrusion force-displacement relationship for a selected alkali-activated fly ash-based
352 paste ($F_{70}L_{30}$) subjected to different ram velocities, for different L_d/D_d ratios (9 and 3.33). An instantaneous
353 increase in force is experienced because of the upsetting of the paste before its exits through the die. The
354 pressure drops correspond to the changes in ram velocity, and the force plateau for each ram velocity is
355 considered to be the corresponding extrusion force. The significant influence of L_d/D_d ratio on the
356 extrusion force is shown in Figure 11, which can be used to glean the importance of the extruder geometry
357 for desirable extrusion-related parameters.



358

359 Figure 11: Force vs. ram displacement for a printable paste in a syringe extruder subjected to different
360 ram velocities.

361 The Benbow-Bridgwater model can be expressed as:

$$P_{ext} = P_1 + P_2 = (\sigma_0 + \alpha V_{ext}^m) \ln\left(\frac{A_b}{A_d}\right) + \frac{ML}{A_d}(\tau_0 + \beta V_{ext}^n) = \sigma_Y \ln\left(\frac{A_b}{A_d}\right) + \frac{ML}{A_d} \tau_w \quad (3)$$

where P_{ext} is the total extrusion pressure, P_1 is the die entry pressure (the pressure required to extrude the paste from the barrel through the die entry), and P_2 is the die land pressure (which allows the paste to flow through the die under pure shear conditions). V_{ext} is the extrusion velocity, α and β are velocity multipliers, and m and n are velocity exponents. σ_0 is the extrusion yield stress (as opposed to pure shear yield stress, since the confinement effects of the barrel and the compressional effects of the ram influence yielding) at the die entry, σ_Y is the apparent velocity-dependent extrusion yield stress of the plastic material, τ_0 is the slip yield stress, and τ_w is the velocity-dependent shear stress experienced by the paste due to its interaction with the die wall. The geometrical parameters include M , L , A_b and A_d which are the perimeter of the die, length of the die, barrel area, and die area respectively. The exponents m and n are taken as 1 (i.e., the extrusion pressure-velocity relationship is taken as linear, which was observed here, as well as in [20]), and thus the equation is reduced to a four-parameter model.

The Benbow-Bridgewater equation was derived based on a uniform die diameter. However, the die geometry used in this study is the frustum of a cone ($D_{entry} \neq D_d$). In this case, the area of die is a function of length of the die and the second term corresponding to the die in Equation 3 is modified suitably [20] as:

$$P_2 = P_{ext} - P_1 = \frac{ML}{A_d}(\tau_0 + \beta V_{ext}^n) = \sum_{i=0}^n \frac{M_i}{A_i} L_i (\tau_w) \quad (4)$$

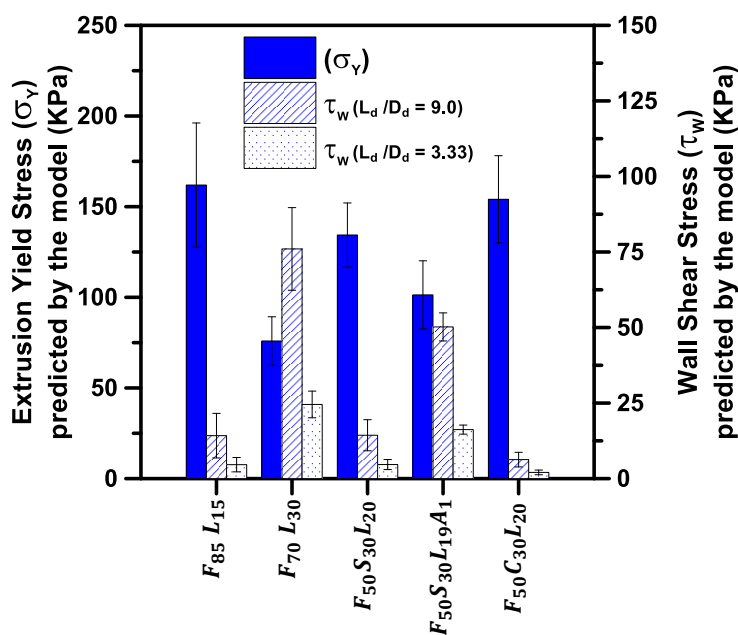
$M_i L_i$ is the surface area of the individual cylinder that forms part of the frustum, and A_i is the cross-sectional area of the cylinder. L_i is taken as 1 mm.

To determine the Benbow-Bridgewater parameters, the extrusion force is plotted as a function of L_d/D_d ratios for different ram velocities. The linear relationship between L_d/D_d and the extrusion force for different velocities is extrapolated back to the Y-axis to give the force at $L_d/D_d = 0$, from which the die entry pressure P_1 for different velocities are calculated. P_1 , along with the barrel and die areas, is used to calculate the velocity-dependent yield stress σ_Y . The wall shear stress τ_w is determined from Equation 4.

Figure 12 depicts the extrusion yield stress (σ_Y) and the wall shear stress (τ_w) predicted by Benbow-Bridgewater model, which can be considered as the extrusion process-related parameters since they are dependent on extrusion velocity. The size of the error bars in this figure show the stresses corresponding to the highest and lowest extrusion velocities (which are deduced from ram velocities) used. The extrusion yield stresses predicted from the model range from 75-to-162 KPa while the shear yield stresses extracted

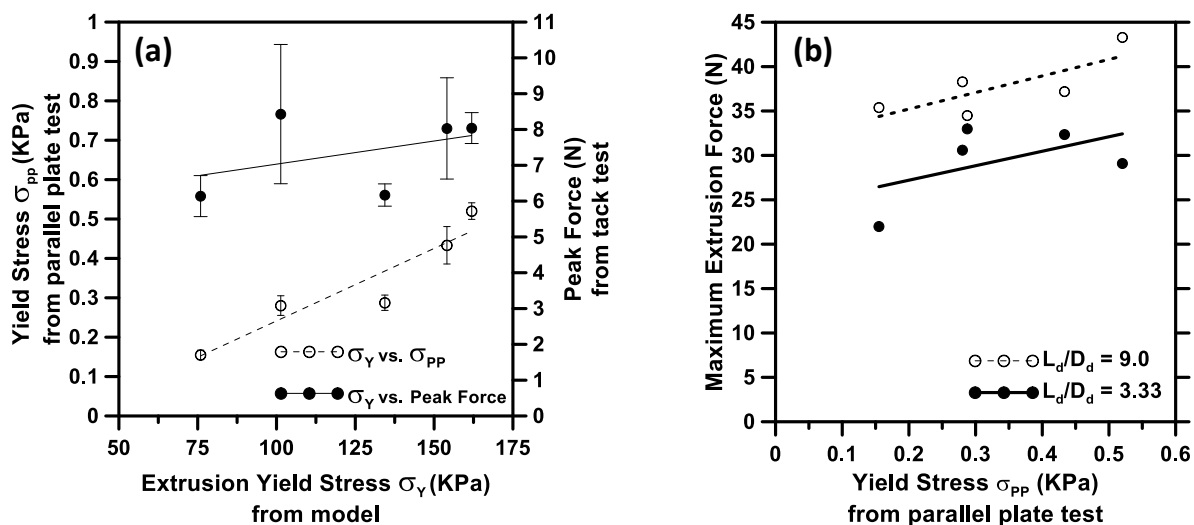
391 through parallel plate rheology ranged from 155-to-520 Pa. Shear yield stress of 50-to-200 Pa measured
 392 through rotational rheology has been correlated to yield stress in the 3-to-40 KPa range from extrusion
 393 experiments [63]. The influence of the extrusion process on rheological response of pastes are thus
 394 evident. To achieve shape stability, it has been reported that the yield stress of extruded paste should be
 395 greater than 20 kPa [64]. All the alkali-activated fly ash-based pastes satisfy this criterion.

396 Wall slip shear stress is an important parameter in 3D printing of binders since this stress must be
 397 surmounted to ensure flow out of the nozzle. The wall shear stress, which is also pressure dependent as
 398 is known for other concentrated suspensions [65–67], depends on the L_d/D_d ratio as can be noticed from
 399 Figure 12, showing that it is. It is seen from this figure that the $F_{70}L_{30}$ mixture shows a higher wall shear
 400 stress notwithstanding a smaller extrusion yield stress. This could potentially be due significant changes
 401 in the paste during the extrusion process (e.g., liquid phase migration) leading to inhomogeneous particle
 402 distribution in the die. The consequence is a higher energy need for extrusion and printing, likely resulting
 403 in further phase separation and inhomogeneous print quality. Extensional and wall stresses predicted
 404 through models thus serve as important tools in the apriori determination of the effectiveness of chosen
 405 mixture compositions and extruder geometry in ensuring efficient extrudability and printability.



406
 407 Figure 12: Velocity-dependent extrusion yield stress and wall shear stress (at two L_d/D_d ratios) for the
 408 printable pastes. The error bars relate to the range of stresses corresponding to the range of extrusion
 409 velocities.

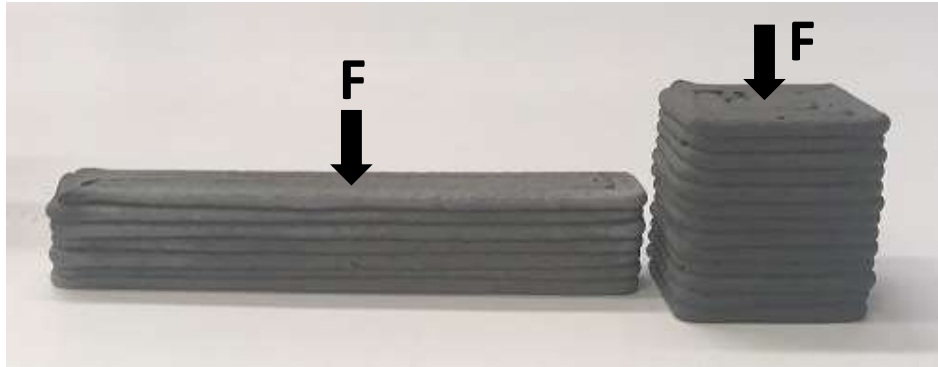
410 Figure 13(a) depicts the relationship between the extrusion yield stress and the shear yield stress
 411 determined from parallel plate rheology and the peak force from tack test. For the selected mixtures, the
 412 extrusion yield stress from extrusion rheology and the shear yield stress from parallel plate rheology are
 413 well correlated, indicating that the determination of simple shear yield stress indeed can be used to infer
 414 the behavior of the paste under extrusion. The tack force and the extrusion yield stress are also well
 415 correlated. It can be postulated that the adhesive forces because of the viscous nature of the mixture in
 416 the presence of activators (as explained earlier) keeps the particles closer together, which consequently
 417 results in an increased extrusion yield stress for the mixtures exhibiting higher tack force. Figure 13(b)
 418 depicts the relationship between the shear yield stress from parallel plate rheology and the extrusion
 419 force required. The extrusion force is taken as the force corresponding to the highest point in the force-
 420 displacement relationship shown in Figure 11. These relationships can be useful in understanding the
 421 extrusion response of these binder systems from straightforward laboratory tests.



422
 423 Figure 13: Correlation of: (a) extrusion yield stress with shear yield stress from parallel plate and peak
 424 force from tack test, and (b) shear yield stress from parallel plate with force of extrusion.

425 3.4 Compressive and Flexural Strengths of 3D-Printed Binders

426 The compressive and flexural strengths of the alkali-activated fly ash-based 3D printed cubes and beams
 427 were evaluated after the respective curing regimes. In the first curing regime, all the samples were cured
 428 in a moist chamber ($23 \pm 1^\circ\text{C}$, $> 98\% \text{RH}$) until 28 days. In the second regime, all the samples except the
 429 mixture containing OPC ($F_{50}C_{30}L_{20}$) were exposed to heat curing (at 70°C) for two different durations (24 h
 430 and 48 h). Figure 14 shows the test directions. Three companion specimens were used for compressive
 431 and flexural strength testing.



432

433

Figure 14: The test direction for mechanical strengths.

434

435

436

437

438

439

440

441

442

443

444

445

Figure 15 depicts the compressive and flexural strengths of the selected binders. When moist cured, the compressive strength increases with reducing amount of fly ash in the binder, as expected. The compressive strength of the paste containing OPC is the highest. Similar strengths have been attained for mixtures containing high volumes of fly ash, activated using alkali sulfates [38]. The 28-day compressive strength the $F_{50}S_{30}L_{20}$ mixture activated using NaOH was lower than that of $F_{50}S_{30}L_{19}A_1$ mixture activated using sodium silicate, owing to the presence of reactive silica from the sodium silicate leading to enhancement in the reaction product volume and constitution. The fly ash-limestone specimens ($F_{85}L_{15}$ and $F_{70}L_{30}$) cured at ($23 \pm 1^\circ\text{C}$, $> 98\% \text{ RH}$) and tested at 28-day showed the lowest compressive strength among the test specimens. The compressive strengths of the $F_{85}L_{15}$ and $F_{70}L_{30}$ mixtures activated using NaOH improved when cured at 70°C , with a longer curing duration providing better strengths. The compressive strength results of 3D printed binders shown here suggest that the trends are similar to the compressive strengths of binders cast in a conventional manner [38,68].

446

447

448

449

450

451

452

453

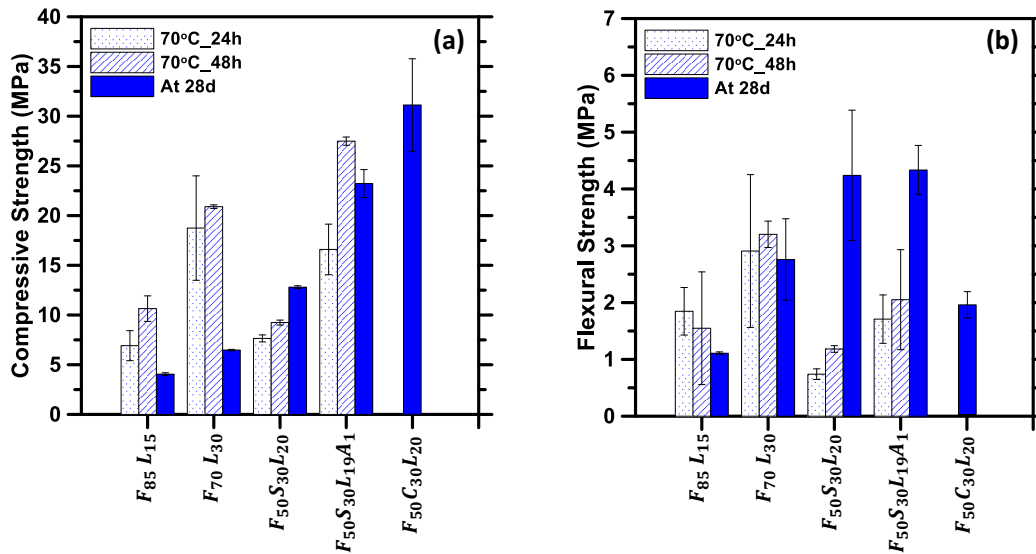
454

455

Figure 15(b) depicts the flexural strength of the 3D printed alkali activated fly ash-based binders. For the $F_{85}L_{15}$ and $F_{70}L_{30}$ mixtures, the heat treatment improved the flexural strength when compared to the moist curing regime. However, the heat treatment was found to cause extensive microcracking in the $F_{50}S_{30}L_{20}$ and $F_{50}S_{30}L_{19}A_1$ mixtures due to the high shrinkage of slag-containing alkali activated binders [69,70], thereby leading to poor flexural strength (microcracking influences flexural strength more than the compressive strength). The slag-containing specimens moist-cured at ambient temperatures showed the highest flexural strengths. When shrinkage is countered through moist curing, and the reaction of slag is facilitated, better strengths are obtained. The flexural strength of the OPC-containing mixture was also found to be lower since the interfacial strength of this mixture (as evidenced from tack test results) likely is lower, resulting in interlayer failure at relatively lower flexural stresses. Also, $F_{85}L_{15}$ and $F_{50}C_{30}L_{20}$ showed

456 a higher modulus (peak force to displacement ratio) from the tack test and relatively lower flexural
 457 strengths. This complements previous observations where higher modulus resulted in lower inter-layer
 458 bond strength [56]. More studies on this aspect is ongoing.

459



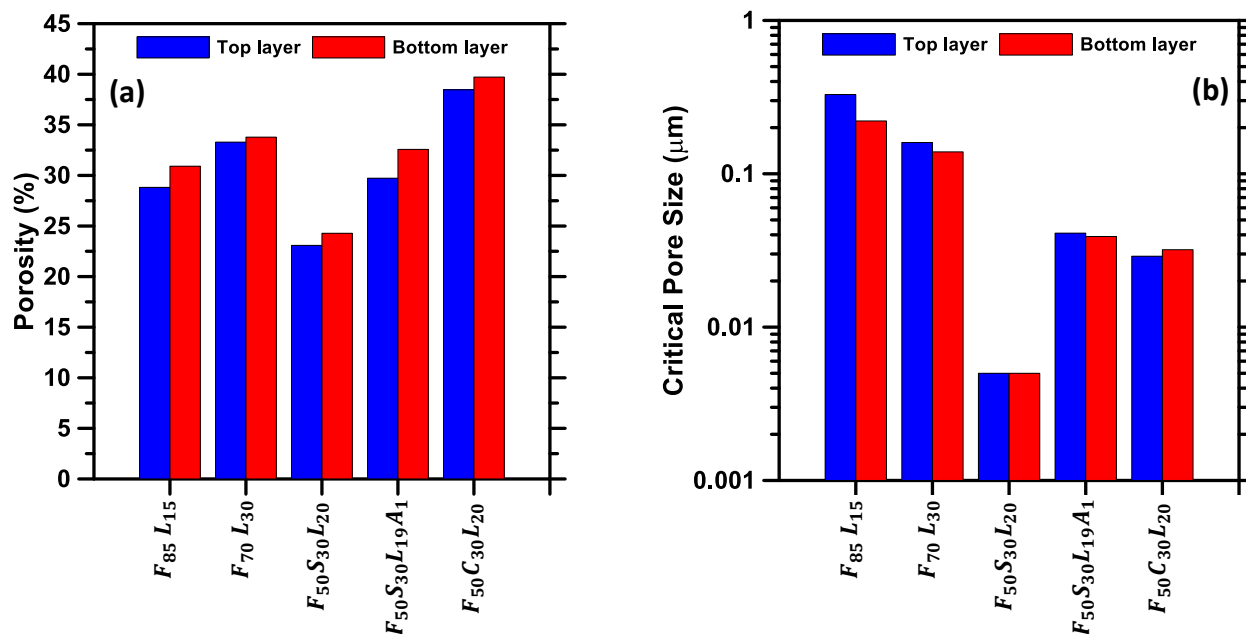
460

461 Figure 15: (a) Compressive strengths, and (b) flexural strengths of selected binders after subjecting to
 462 different curing regimes.

463 3.5 Effect of Extrusion and Overburden Pressure on Pore Structure

464 Layer-wise printing of cementitious composites can impact the pore structure (and thus the mechanical
 465 and durability properties) in multiple ways. The effect of extrusion (consolidation) is not uniform during
 466 the time the paste makes its way out of the extruder, resulting in differing particle concentrations and
 467 fluid contents (due to potential liquid phase migration). When printed in layers, the bottom layer is
 468 subjected to increased overburden pressure from the subsequently printed layers. The specific gravity,
 469 porosity, and critical pore size of the top and bottom layers of the printed cubes (layer dimensions of 6
 470 mm x 3 mm; width x height) are compared in this section. Figure 16 depicts these pore structure
 471 parameters for the pastes studied. The variation in specific gravities between the top and bottom layers
 472 was less than 3% for all the pastes. It is observed that no significant difference exists in the porosity and
 473 critical pore size between the top and bottom layers for all the specimens. The bottom layer, which is
 474 printed first, is generally less influenced by the squeeze and consolidation effects because the material
 475 flows only a small distance before being extruded; however, the overburden pressure in this layer is
 476 higher. For the top layer, there is no overburden pressure, but the paste that constitutes this layer is

477 subjected to higher confinement effects in the barrel and gets subjected to pressure for a longer time
 478 while being extruded. It is thus likely that the net effect on the pastes is rather similar for the extruder
 479 geometry and mixture compositions evaluated here, resulting in insignificant changes in porosity between
 480 the top and bottom layers.



481
 482 Figure 16: (a) Porosity and (b) critical pore sizes of top and bottom layers of the printed cubes.

483 **4. Conclusions**

484 The focus of this paper was on the material design and evaluation of 3D-printable binders based on alkali
 485 activation of fly ash-based blends. Using fly ash as the major ingredient, and limestone, slag, or OPC as
 486 minor ingredients, mixtures were proportioned so as to be **extrudable and buildable (printable)**. When
 487 alkaline activators were used in lieu of water, the shear yield stress of the fresh pastes decreased, and the
 488 cohesiveness increased, similar to the use of a superplasticizer in conventional OPC systems. The yield
 489 stress was also found to depend on the particle sizes (and in turn particle packing in the suspension) of
 490 the constituents. The mini slump values and shear yield stresses determined on extrudable mixtures were
 491 synergistically used to arrive at bounds for printability of the paste mixtures. This study also defined a
 492 printability window based on concurrent measurement of time-dependent yield stress and extrusion
 493 printing of a filament of the paste. For the mixtures evaluated, a shear yield stress of 700 Pa (in parallel
 494 plate rheometry) indicated an upper limit of printability. This window was found to scale relatively well
 495 with the setting time of the pastes. The presence of alkaline activator also resulted in increased tack force
 496 and adhesive energy for these binders as compared to conventional cement-based binders.

497 The extrusion rheology experiments coupled with the Benbow-Bridgwater model facilitated the extraction
498 of extrusion yield stress and die wall slip shear stress of alkali-activated fly ash-based binders, which are
499 important process-related parameters in extrusion-based 3D printing. **These parameters were shown to
500 be related to shear yield stress and extensional (tack) properties of the virgin paste, thereby providing a
501 means to understand the response of the extruded mixture from simple rheological experiments, and
502 therefore could be used to link material design to the extrusion-based printing process.** The compressive
503 and flexural strength tests on the pastes showed that, in general, comparable mechanical properties as
504 that of conventionally cast specimens can be obtained through layered printing. However, strength
505 reduction likely due to microcracking (for mixtures containing slag, especially when heat cured) and weak
506 inter-layer bonding (in mixtures containing portland cement) were observed, which requires careful
507 material design and curing conditions to ensure long-term performance and durability. The study has
508 shown that alkali activated fly ash-based binders can be successfully designed for beneficial properties.

509 **5. Acknowledgments**

510 The authors sincerely acknowledge support from National Science Foundation (CMMI: 1727445) towards
511 the conduct of this study. The contents of this paper reflect the views of the authors who are responsible
512 for the facts and accuracy of the data presented herein, and do not necessarily reflect the views and
513 policies of NSF, nor do the contents constitute a standard, specification or a regulation. We gratefully
514 acknowledge the use of facilities within Laboratory for the Science of Sustainable Infrastructural Materials
515 (LS-SIM) at Arizona State University.

516 **6. Data Availability**

517 The raw/processed data required to reproduce these findings cannot be shared at this time as the data
518 also forms part of an ongoing study.

519 **7. References**

- 520 [1] J. Malda, J. Visser, F.P. Melchels, T. Jüngst, W.E. Hennink, W.J.A. Dhert, J. Groll, D.W. Hutmacher,
521 25th Anniversary Article: Engineering Hydrogels for Biofabrication, *Advanced Materials*. 25 (2013)
522 5011–5028. doi:10.1002/adma.201302042.
- 523 [2] S.V. Murphy, A. Atala, 3D bioprinting of tissues and organs, *Nature Biotechnology*. 32 (2014) 773–
524 785. doi:10.1038/nbt.2958.
- 525 [3] V. Petrovic, J.V.H. Gonzalez, O.J. Ferrando, J.D. Gordillo, J.R.B. Puchades, L.P. Griñan, Additive
526 layered manufacturing: sectors of industrial application shown through case studies, *International
527 Journal of Production Research*. 49 (2011) 1061–1079. doi:10.1080/00207540903479786.

- 528 [4] T.J. Horn, O.L.A. Harrysson, Overview of current additive manufacturing technologies and selected
529 applications, *Science Progress*; St Albans. 95 (2012) 255.
530 doi:<http://dx.doi.org.ezproxy1.lib.asu.edu/10.3184/003685012X13420984463047>.
- 531 [5] R. Bogue, 3D printing: the dawn of a new era in manufacturing?, *Assembly Automation*. 33 (2013)
532 307–311. doi:10.1108/AA-06-2013-055.
- 533 [6] P. Wu, J. Wang, X. Wang, A critical review of the use of 3-D printing in the construction industry,
534 *Automation in Construction*. 68 (2016) 21–31. doi:10.1016/j.autcon.2016.04.005.
- 535 [7] G. De Schutter, K. Lesage, V. Mechtcherine, V.N. Nerella, G. Habert, I. Agusti-Juan, Vision of 3D
536 printing with concrete — Technical, economic and environmental potentials, *Cement and Concrete*
537 *Research*. 112 (2018) 25–36. doi:10.1016/j.cemconres.2018.06.001.
- 538 [8] R.A. Buswell, W.R. Leal de Silva, S.Z. Jones, J. Dirrenberger, 3D printing using concrete extrusion: A
539 roadmap for research, *Cement and Concrete Research*. 112 (2018) 37–49.
540 doi:10.1016/j.cemconres.2018.05.006.
- 541 [9] D. Asprone, F. Auricchio, C. Menna, V. Mercuri, 3D printing of reinforced concrete elements:
542 Technology and design approach, *Construction and Building Materials*. 165 (2018) 218–231.
543 doi:10.1016/j.conbuildmat.2018.01.018.
- 544 [10] I. Hager, A. Golonka, R. Putanowicz, 3D Printing of Buildings and Building Components as the Future
545 of Sustainable Construction?, *Procedia Engineering*. 151 (2016) 292–299.
546 doi:10.1016/j.proeng.2016.07.357.
- 547 [11] A.K. Singh, B. Patil, N. Hoffmann, B. Saltonstall, M. Doddamani, N. Gupta, Additive Manufacturing of
548 Syntactic Foams: Part 1: Development, Properties, and Recycling Potential of Filaments, *JOM*. 70
549 (2018) 303–309. doi:10.1007/s11837-017-2734-7.
- 550 [12] A.K. Singh, B. Saltonstall, B. Patil, N. Hoffmann, M. Doddamani, N. Gupta, Additive Manufacturing of
551 Syntactic Foams: Part 2: Specimen Printing and Mechanical Property Characterization, *JOM*. 70
552 (2018) 310–314. doi:10.1007/s11837-017-2731-x.
- 553 [13] C. Gosselin, R. Duballet, P. Roux, N. Gaudillière, J. Dirrenberger, P. Morel, Large-scale 3D printing of
554 ultra-high performance concrete – a new processing route for architects and builders, *Materials &*
555 *Design*. 100 (2016) 102–109. doi:10.1016/j.matdes.2016.03.097.
- 556 [14] M. Hambach, D. Volkmer, Properties of 3D-printed fiber-reinforced Portland cement paste, *Cement*
557 *and Concrete Composites*. 79 (2017) 62–70. doi:10.1016/j.cemconcomp.2017.02.001.
- 558 [15] A. Kazemian, X. Yuan, E. Cochran, B. Khoshnevis, Cementitious materials for construction-scale 3D
559 printing: Laboratory testing of fresh printing mixture, *Construction and Building Materials*. 145
560 (2017) 639–647. doi:10.1016/j.conbuildmat.2017.04.015.
- 561 [16] M. Xia, B. Nematollahi, J. Sanjayan, Compressive Strength and Dimensional Accuracy of Portland
562 Cement Mortar Made Using Powder-Based 3D Printing for Construction Applications, in: *First RILEM*
563 *International Conference on Concrete and Digital Fabrication – Digital Concrete 2018*, Springer,
564 Cham, 2018: pp. 245–254. doi:10.1007/978-3-319-99519-9_23.
- 565 [17] P. Shakor, J. Sanjayan, A. Nazari, S. Nejadi, Modified 3D printed powder to cement-based material
566 and mechanical properties of cement scaffold used in 3D printing, *Construction and Building*
567 *Materials*. 138 (2017) 398–409. doi:10.1016/j.conbuildmat.2017.02.037.
- 568 [18] M. Moini, J. Olek, J.P. Youngblood, B. Magee, P.D. Zavattieri, Additive Manufacturing and
569 Performance of Architected Cement-Based Materials, *Advanced Materials*. 0 (2018) 1802123.
570 doi:10.1002/adma.201802123.
- 571 [19] Y. Zhang, Y. Zhang, G. Liu, Y. Yang, M. Wu, B. Pang, Fresh properties of a novel 3D printing concrete
572 ink, *Construction and Building Materials*. 174 (2018) 263–271.
573 doi:10.1016/j.conbuildmat.2018.04.115.

- 574 [20] S. A.O. Nair, H. Alghamdi, A. Arora, I. Mehdipour, G. Sant, N. Neithalath, Linking Fresh Paste
575 Microstructure, Rheology and Extrusion Characteristics of Cementitious Binders for 3D Printing,
576 Journal of the American Ceramic Society (under review). (2018).
- 577 [21] N. Roussel, Rheological requirements for printable concretes, Cement and Concrete Research. 112
578 (2018) 76–85. doi:10.1016/j.cemconres.2018.04.005.
- 579 [22] F. Bos, R. Wolfs, Z. Ahmed, T. Salet, Additive manufacturing of concrete in construction: potentials
580 and challenges of 3D concrete printing, Virtual and Physical Prototyping. 11 (2016) 209–225.
581 doi:10.1080/17452759.2016.1209867.
- 582 [23] R.J.M. Wolfs, F.P. Bos, T.A.M. Salet, Early age mechanical behaviour of 3D printed concrete:
583 Numerical modelling and experimental testing, Cement and Concrete Research. 106 (2018) 103–
584 116. doi:10.1016/j.cemconres.2018.02.001.
- 585 [24] A. Perrot, D. Rangeard, A. Pierre, Structural built-up of cement-based materials used for 3D-printing
586 extrusion techniques, Mater Struct. 49 (2016) 1213–1220. doi:10.1617/s11527-015-0571-0.
- 587 [25] T.T. Le, S.A. Austin, S. Lim, R.A. Buswell, A.G.F. Gibb, T. Thorpe, Mix design and fresh properties for
588 high-performance printing concrete, Mater Struct. 45 (2012) 1221–1232. doi:10.1617/s11527-012-
589 9828-z.
- 590 [26] A. Pierre, D. Weger, A. Perrot, D. Lowke, Penetration of cement pastes into sand packings during 3D
591 printing: analytical and experimental study, Mater Struct. 51 (2018) 22. doi:10.1617/s11527-018-
592 1148-5.
- 593 [27] C. Gosselin, R. Duballet, P. Roux, N. Gaudillière, J. Dirrenberger, P. Morel, Large-scale 3D printing of
594 ultra-high performance concrete – a new processing route for architects and builders, Materials &
595 Design. 100 (2016) 102–109. doi:10.1016/j.matdes.2016.03.097.
- 596 [28] M. Xia, J. Sanjayan, Method of formulating geopolymer for 3D printing for construction applications,
597 Materials & Design. 110 (2016) 382–390. doi:10.1016/j.matdes.2016.07.136.
- 598 [29] B. Panda, S.C. Paul, L.J. Hui, Y.W.D. Tay, M.J. Tan, Additive manufacturing of geopolymer for
599 sustainable built environment, Journal of Cleaner Production. 167 (2017) 281–288.
600 doi:10.1016/j.jclepro.2017.08.165.
- 601 [30] B. Panda, S.C. Paul, N.A.N. Mohamed, Y.W.D. Tay, M.J. Tan, Measurement of tensile bond strength
602 of 3D printed geopolymer mortar, Measurement. 113 (2018) 108–116.
603 doi:10.1016/j.measurement.2017.08.051.
- 604 [31] B. Panda, C. Unluer, M.J. Tan, Investigation of the rheology and strength of geopolymer mixtures for
605 extrusion-based 3D printing, Cement and Concrete Composites. 94 (2018) 307–314.
606 doi:10.1016/j.cemconcomp.2018.10.002.
- 607 [32] B. Panda, M.J. Tan, Experimental study on mix proportion and fresh properties of fly ash based
608 geopolymer for 3D concrete printing, Ceramics International. 44 (2018) 10258–10265.
609 doi:10.1016/j.ceramint.2018.03.031.
- 610 [33] J. Sun, W. Zhou, L. Yan, D. Huang, L. Lin, Extrusion-based food printing for digitalized food design
611 and nutrition control, Journal of Food Engineering. 220 (2018) 1–11.
612 doi:10.1016/j.jfoodeng.2017.02.028.
- 613 [34] Slic3r, (2017). <http://slic3r.org/>.
- 614 [35] R.J. Flatt, P. Bowen, Yodel: A Yield Stress Model for Suspensions, Journal of the American Ceramic
615 Society. 89 (2006) 1244–1256. doi:10.1111/j.1551-2916.2005.00888.x.
- 616 [36] K. Vance, A. Arora, G. Sant, N. Neithalath, Rheological evaluations of interground and blended
617 cement–limestone suspensions, Construction and Building Materials. 79 (2015) 65–72.
618 doi:10.1016/j.conbuildmat.2014.12.054.
- 619 [37] K. Vance, A. Dakhane, G. Sant, N. Neithalath, Observations on the rheological response of alkali
620 activated fly ash suspensions: the role of activator type and concentration, Rheol Acta. 53 (2014)
621 843–855. doi:10.1007/s00397-014-0793-z.

- 622 [38] A. Dakhane, S. Tweedley, S. Kailas, R. Marzke, N. Neithalath, Mechanical and microstructural
623 characterization of alkali sulfate activated high volume fly ash binders, *Materials & Design*. 122
624 (2017) 236–246. doi:10.1016/j.matdes.2017.03.021.
- 625 [39] K. Vance, G. Sant, N. Neithalath, The rheology of cementitious suspensions: A closer look at
626 experimental parameters and property determination using common rheological models, *Cement
627 and Concrete Composites*. 59 (2015) 38–48. doi:10.1016/j.cemconcomp.2015.03.001.
- 628 [40] P. Bosscher, R.L. Williams, L.S. Bryson, D. Castro-Lacouture, Cable-suspended robotic contour
629 crafting system, *Automation in Construction*. 17 (2007) 45–55. doi:10.1016/j.autcon.2007.02.011.
- 630 [41] ASTM C 191-13, Standard Test Methods for Time of Setting of Hydraulic Cement by Vicat Needle,
631 ASTM International. (2013).
- 632 [42] T. Bakharev, Thermal behaviour of geopolymers prepared using class F fly ash and elevated
633 temperature curing, *Cement and Concrete Research*. 36 (2006) 1134–1147.
634 doi:10.1016/j.cemconres.2006.03.022.
- 635 [43] K. Okada, A. Ooyama, T. Isobe, Y. Kameshima, A. Nakajima, K.J.D. MacKenzie, Water retention
636 properties of porous geopolymers for use in cooling applications, *Journal of the European Ceramic
637 Society*. 29 (2009) 1917–1923. doi:10.1016/j.jeurceramsoc.2008.11.006.
- 638 [44] P. Rovnanik, Effect of curing temperature on the development of hard structure of metakaolin-
639 based geopolymer, *Construction and Building Materials*. 24 (2010) 1176–1183.
640 doi:10.1016/j.conbuildmat.2009.12.023.
- 641 [45] T. Lin, D. Jia, P. He, M. Wang, D. Liang, Effects of fiber length on mechanical properties and fracture
642 behavior of short carbon fiber reinforced geopolymer matrix composites, *Materials Science and
643 Engineering: A*. 497 (2008) 181–185. doi:10.1016/j.msea.2008.06.040.
- 644 [46] K. Vance, A. Dakhane, G. Sant, N. Neithalath, Observations on the rheological response of alkali
645 activated fly ash suspensions: the role of activator type and concentration, *Rheol Acta*. 53 (2014)
646 843–855. doi:10.1007/s00397-014-0793-z.
- 647 [47] P. Nath, P.K. Sarker, Effect of GGBFS on setting, workability and early strength properties of fly ash
648 geopolymer concrete cured in ambient condition, *Construction and Building Materials*. 66 (2014)
649 163–171. doi:10.1016/j.conbuildmat.2014.05.080.
- 650 [48] P. Chindaprasirt, P.D. Silva, K. Sagoe-Crentsil, S. Hanjitsuwan, Effect of SiO₂ and Al₂O₃ on the setting
651 and hardening of high calcium fly ash-based geopolymer systems, *J Mater Sci*. 47 (2012) 4876–4883.
652 doi:10.1007/s10853-012-6353-y.
- 653 [49] T. Lecompte, A. Perrot, Non-linear modeling of yield stress increase due to SCC structural build-up at
654 rest, *Cement and Concrete Research*. 92 (2017) 92–97. doi:10.1016/j.cemconres.2016.11.020.
- 655 [50] Z. Zhou, M.J. Solomon, P.J. Scales, D.V. Boger, The yield stress of concentrated flocculated
656 suspensions of size distributed particles, *Journal of Rheology*. 43 (1999) 651–671.
657 doi:10.1122/1.551029.
- 658 [51] R.J.M. Wolfs, F.P. Bos, T.A.M. Salet, Early age mechanical behaviour of 3D printed concrete:
659 Numerical modelling and experimental testing, *Cement and Concrete Research*. 106 (2018) 103–
660 116. doi:10.1016/j.cemconres.2018.02.001.
- 661 [52] Z. Tan, S.A. Bernal, J.L. Provis, Reproducible mini-slump test procedure for measuring the yield
662 stress of cementitious pastes, *Mater Struct*. 50 (2017) 235. doi:10.1617/s11527-017-1103-x.
- 663 [53] C. Lu, H. Yang, G. Mei, Relationship between slump flow and rheological properties of self
664 compacting concrete with silica fume and its permeability, *Construction and Building Materials*. 75
665 (2015) 157–162. doi:10.1016/j.conbuildmat.2014.08.038.
- 666 [54] S. Kawashima, M. Chaouche, D.J. Corr, S.P. Shah, Influence of purified attapulgite clays on the
667 adhesive properties of cement pastes as measured by the tack test, *Cement and Concrete
668 Composites*. 48 (2014) 35–41. doi:10.1016/j.cemconcomp.2014.01.005.

- 669 [55] A. Kaci, R. Bouras, V.T. Phan, P.A. Andréani, M. Chaouche, H. Brossas, Adhesive and rheological
670 properties of fresh fibre-reinforced mortars, *Cement and Concrete Composites*. 33 (2011) 218–224.
671 doi:10.1016/j.cemconcomp.2010.10.009.
- 672 [56] Y.W.D. Tay, G.H.A. Ting, Y. Qian, B. Panda, L. He, M.J. Tan, Time gap effect on bond strength of 3D-
673 printed concrete, *Virtual and Physical Prototyping*. 14 (2019) 104–113.
674 doi:10.1080/17452759.2018.1500420.
- 675 [57] A. Perrot, C. Lanos, P. Estellé, Y. Melinge, Ram extrusion force for a frictional plastic material: model
676 prediction and application to cement paste, *Rheol Acta*. 45 (2006) 457–467. doi:10.1007/s00397-
677 005-0074-y.
- 678 [58] C. Ness, J.Y. Ooi, J. Sun, M. Marigo, P. McGuire, H. Xu, H. Stitt, Linking particle properties to dense
679 suspension extrusion flow characteristics using discrete element simulations, *AIChE Journal*. 63
680 (2017) 3069–3082. doi:10.1002/aic.15768.
- 681 [59] D.J. Horrobin, R.M. Nedderman, Die entry pressure drops in paste extrusion, *Chemical Engineering
682 Science*. 53 (1998) 3215–3225. doi:10.1016/S0009-2509(98)00105-5.
- 683 [60] R.A. Basterfield, C.J. Lawrence, M.J. Adams, On the interpretation of orifice extrusion data for
684 viscoplastic materials, *Chemical Engineering Science*. 60 (2005) 2599–2607.
685 doi:10.1016/j.ces.2004.12.019.
- 686 [61] J. Benbow, J. Bridgwater, *Paste flow and extrusion*, Clarendon Press, Oxford, UK. (1993).
- 687 [62] J. Powell, S. Assabumrungrat, S. Blackburn, Design of ceramic paste formulations for co-extrusion,
688 *Powder Technology*. 245 (2013) 21–27. doi:10.1016/j.powtec.2013.04.017.
- 689 [63] P.F.G. Banfill, *Rheology of Fresh Cement and Concrete: Proceedings of an International Conference*,
690 Liverpool, 1990, CRC Press, 1990.
- 691 [64] D. Konigsberg, T.M. Nicholson, P.J. Halley, T.J. Kealy, P.K. Bhattacharjee, Online process rheometry
692 using oscillatory squeeze flow, *Applied Rheology*. 23 (2013). doi:10.3933/AppRheol-23-35688.
- 693 [65] M.P. Bryan, S.L. Rough, D.I. Wilson, Measurement of the wall slip behaviour of a solid granular soap
694 in ram extrusion, *Powder Technology*. 323 (2018) 76–85. doi:10.1016/j.powtec.2017.09.053.
- 695 [66] C.W. Stewart, Wall slip in the extrusion of linear polyolefins, *Journal of Rheology*. 37 (1993) 499–
696 513. doi:10.1122/1.550456.
- 697 [67] P. Ballesta, R. Besseling, L. Isa, G. Petekidis, W.C.K. Poon, Slip and Flow of Hard-Sphere Colloidal
698 Glasses, *Phys. Rev. Lett.* 101 (2008) 258301. doi:10.1103/PhysRevLett.101.258301.
- 699 [68] D. Ravikumar, S. Peethamparan, N. Neithalath, Structure and strength of NaOH activated concretes
700 containing fly ash or GGBFS as the sole binder, *Cement and Concrete Composites*. 32 (2010) 399–
701 410. doi:10.1016/j.cemconcomp.2010.03.007.
- 702 [69] H. Ye, A. Radlińska, Shrinkage mechanisms of alkali-activated slag, *Cement and Concrete Research*.
703 88 (2016) 126–135. doi:10.1016/j.cemconres.2016.07.001.
- 704 [70] N.K. Lee, J.G. Jang, H.K. Lee, Shrinkage characteristics of alkali-activated fly ash/slag paste and
705 mortar at early ages, *Cement and Concrete Composites*. 53 (2014) 239–248.
706 doi:10.1016/j.cemconcomp.2014.07.007.
- 707